

## Micro-computed tomography analysis of ring, rotor, and air jet yarn structures and their impact on fragmented fibres release from polyester textiles

Abdul Jabbar, Haoqi Zhang, Dongmin Yang, Elizabeth Evans & Muhammad Tausif

To cite this article: Abdul Jabbar, Haoqi Zhang, Dongmin Yang, Elizabeth Evans & Muhammad Tausif (25 Mar 2025): Micro-computed tomography analysis of ring, rotor, and air jet yarn structures and their impact on fragmented fibres release from polyester textiles, *Nondestructive Testing and Evaluation*, DOI: [10.1080/10589759.2025.2482868](https://doi.org/10.1080/10589759.2025.2482868)

To link to this article: <https://doi.org/10.1080/10589759.2025.2482868>



© 2025 The Author(s). Published by Informa UK Limited, trading as Taylor & Francis Group.



Published online: 25 Mar 2025.



Submit your article to this journal [↗](#)



Article views: 153



View related articles [↗](#)



View Crossmark data [↗](#)

# Micro-computed tomography analysis of ring, rotor, and air jet yarn structures and their impact on fragmented fibres release from polyester textiles

Abdul Jabbar<sup>a,b</sup>, Haoqi Zhang<sup>c</sup>, Dongmin Yang<sup>d</sup>, Elizabeth Evans<sup>e</sup> and Muhammad Tausif<sup>a</sup>

<sup>a</sup>School of Design, University of Leeds, Leeds, UK; <sup>b</sup>Department of Textile Engineering, National Textile University, Faisalabad, Pakistan; <sup>c</sup>School of Advanced Manufacturing, Sun Yat-Sen University, Shenzhen, People's Republic of China; <sup>d</sup>Institute for Materials and Processes, School of Engineering, University of Edinburgh, Edinburgh, UK; <sup>e</sup>Henry Moseley X-ray Imaging Facility, Alan Turing Building, University of Manchester, Manchester, UK

## ABSTRACT

The structural arrangements of fibres in a yarn (bundle of fibres) are critical to its properties. X-ray micro-computed tomography ( $\mu$ CT), an advanced non-destructive technique, was employed to investigate the internal structure of 100% staple PET (polyethylene terephthalate) yarns produced by ring, rotor, and airjet spinning. Commercially relevant yarns of the same linear density were scanned 9 times along their length using  $\mu$ CT to generate stitched 3D reconstructions to analyse fibre arrangements along the yarn length and cross-section. Image-J and Avizo software processed the data, revealing distinct structural differences among yarn types. Ring-spun yarns exhibited rounder profiles, higher fibre packing density, and greater fibre migration, followed by air jet and rotor yarns. A direct relationship between fibre migration (mean fibre position, RMS deviation) and mean packing density with the yarn tensile strength was observed with ring-spun yarn showing the highest values, followed by air jet and rotor yarns. The fragmented fibres (FFs) mass release is explained in terms of structural features of yarns. The yarn hairiness and radial packing density near the yarn periphery were attributed to the release of FFs. This study presents a novel  $\mu$ CT approach, compared to traditional tracer fibre techniques and cross-sectional microtomy, to analyse staple spun yarn structures.

## ARTICLE HISTORY

Received 10 October 2024  
Accepted 17 March 2025

## KEYWORDS

X-ray micro-computed tomography; yarn structure; fibre migration; fibre packing density; fragmented fibres

## 1. Introduction

Staple spun yarns account for approximately 45% of global yarn production [1]. Yarn properties are influenced by both yarn structure and fibre characteristics. The yarn structure, which refers to the geometrical arrangement of fibres in the yarn body, is determined by how the constituent fibres are arranged along their length and cross-section. This arrangement can be described by fibre migration, radial position, and

**CONTACT** Muhammad Tausif  [m.tausif@leeds.ac.uk](mailto:m.tausif@leeds.ac.uk)

© 2025 The Author(s). Published by Informa UK Limited, trading as Taylor & Francis Group.

This is an Open Access article distributed under the terms of the Creative Commons Attribution License (<http://creativecommons.org/licenses/by/4.0/>), which permits unrestricted use, distribution, and reproduction in any medium, provided the original work is properly cited. The terms on which this article has been published allow the posting of the Accepted Manuscript in a repository by the author(s) or with their consent.

packing density [2]. Fibre migration depicts the relative position of a fibre with respect to its neighbouring fibres or the changes in the radial position of fibre elements along the yarn axis. Fibre migration affects the packing and binding of fibres in the yarn [3]. The yarn structure is primarily influenced by the spinning technology used to produce the staple yarn [4]. Among the prominent industrial spun yarn production technologies, ring spinning remains the dominant and oldest technology in the textile industry due to its suitability for a wide range of textile applications [5]. In the last few decades, rotor and air jet spinning technologies have gained widespread commercial acceptance due to their more sustainable manufacturing processes compared to ring spinning [6].

The release of fibrous microplastics, including fragmented fibres (FFs), from textiles constitutes a pressing global environmental issue. Research has identified yarn structure as a key factor contributing to the generation and release of FFs from textiles [7,8]. Enhancing the structural integrity of fibres within a yarn, particularly at its outer perimeter, can significantly reduce surface wear, minimise fibre damage and fuzz formation during a textile's service life. Consequently, this can lead to a substantial decrease in the release of FFs from textiles. Therefore, a comprehensive understanding of yarn structure is essential for informed staple spun yarn selection and engineer textiles during production, as it can directly influence durability, service life, and FFs shedding from textiles.

Theoretically, yarn was considered to consist of a core fibre surrounded by coaxial cylindrical layers of other neighbouring fibres, each forming a perfect helix of constant radius along the yarn length. However, Pierce reported a phenomenon wherein fibres change their positions within a yarn [9]. The introduction of the tracer fibre technique by Morton and Yen [10] further invalidated this theoretical assumption and revealed that fibres are radially positioned with respect to the central axis of the yarn. Additionally, cross-sectional microtomy showed a non-uniform packing density of fibres within the yarn [11]. Over the years, both the tracer fibre [12,13] and yarn cross-sectional microtomy [14,15] techniques have remained well-established traditional methods for structural analysis of yarns. Both methods have undergone various developments in experimental setups to improve yarn structural analysis. Numerous studies have reported on yarn structural analysis over the past several decades using the tracer fibre and yarn cross-section methods. For instance, researchers reported the structural arrangement of fibres in conventional ring [12,16,17], modified ring [16], compact [12,16,18], rotor [17,19], air jet [20] and friction [17] spun yarns by investigating their fibre migration parameters. Similarly, fibre distribution in yarn cross sections and packing densities of ring [13,21], compact [14,21], air jet [2,21] and rotor [11,22] spun yarns were explored by yarn cross section microtomy method.

Despite the widespread acceptance of these methods for structural analysis of yarns, they have certain limitations that hinder their ability to provide a detailed investigation of yarn structure [23]. For instance, the tracer fibre technique only reveals the trajectory of a few fibres from a bundle of tens to hundreds of fibres in a yarn body, depending on its linear density. The cross-sectional method, on the other hand, allows for the capture and analysis of a cross-sectional image of a specific yarn section. However, investigating both longitudinal and cross-sectional fibre arrangements poses a significant challenge, as it is impractical to apply both methodologies to the same yarn specimen section simultaneously. Furthermore, sample preparation during cross-sectional microtomy requires

manual handling during slicing and imaging, which may disturb the delicate distribution of fibres within the yarn, potentially leading to misleading observations. These limitations highlight that there are limitations to elucidate the internal yarn structure and there is a need to explore a suitable non-destructive technique that could help investigate yarn structure by analysing both longitudinal and cross-sectional arrangements of fibres without introduction of a resin in the inter-fibre spaces.

Micro-computed tomography ( $\mu$ CT) has emerged as a novel technique for analysing the internal yarn structure [23–25]. This method has also been applied to the structural analysis of textile fabrics [26,27]. Although computed tomography is primarily used in medicine for medical imaging, its application in exploring the microstructure of materials has significantly increased in Materials Science and Engineering [28]. The  $\mu$ CT is a non-destructive technique in which an object is exposed to X-rays for three-dimensional (3D) scanning to obtain its internal details. During CT scanning, a series of images of a specimen are taken sequentially from all directions to produce 2D sectional images or 3D spatial images. Stacking these CT images together reveals the internal structure of the specimen for further analysis. Thus,  $\mu$ CT overcomes the limitations associated with tracer fibre and microtomy techniques when analysing yarn structures. Moreover,  $\mu$ CT offers advantages of superior spatial and contrast resolution at the submicron level compared to standard CT allowing for better quantitative analysis. It further offers the possibility to examine smaller specimens which are challenging to analyse with standard CT. However, these advantages come with a smaller field of view and longer scanning times compared to standard CT [29]. A recent study has investigated ring-spun yarn structure using  $\mu$ CT and computed various structural parameters related to fibre distribution in the yarn cross-section and fibre arrangement along the yarn length [23]. However, no study in the literature has used  $\mu$ CT to investigate and compare the structures of yarns produced from commercially and industrially relevant spun yarn technologies (i.e. ring, rotor, and air-jet). Therefore, the objective of this study is to explore the internal structure of ring, rotor, and air jet spun yarns using  $\mu$ CT, and relate the release of FFs from their corresponding bespoke textiles (as published in study [8]). Compared to a small proportion of fibres studied by tracer fibre technique, this research further aims to study all fibres and their arrangements along the length and cross-section of yarns from commercially relevant spun yarn technologies, overcoming the shortcomings associated with traditional methods.

## 2. Materials and methods

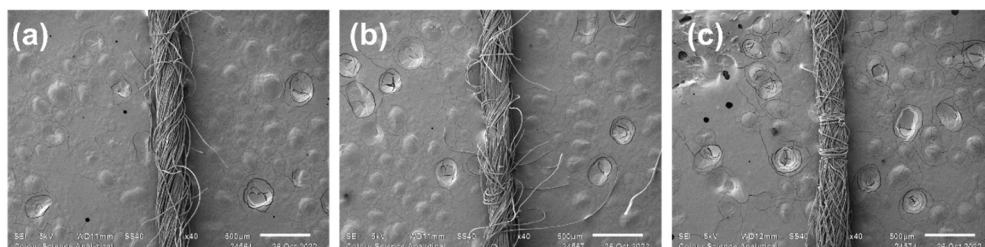
### 2.1. Micro-ct scanning

#### 2.1.1. Samples and scanning set-up

For  $\mu$ CT scanning and microstructural analysis, 100% PET (polyethylene terephthalate) staple-spun yarns from commercially relevant short staple spinning systems – ring, air jet (vortex), and rotor spinning – were selected. The PET staple fibres of 38 mm cut length, and 1.2 denier (1.33 dtex) linear density were spun into yarns of nominal linear density of 29.53 tex (20.0's Ne). The manufacturing details of all spun yarns are reported in study [8]. The twist level in conventional ring-spun yarn was maintained at  $7.04 \text{ turns.cm}^{-1}$

**Table 1.** Physical properties of spun yarns [8].

Sr. No.	Spun Yarn	Actual count (tex)	Unevenness (%)	Total Imperfections/km	Hairiness Index (-)	Zweigle Hairiness, S3
1	Ring	28.56 ± 0.39	10.85 ± 0.63	57.6 ± 19.72	6.29 ± 0.15	1356 ± 185
2	Airjet	29.02 ± 0.17	9.45 ± 0.11	26.5 ± 7.37	3.79 ± 0.03	2.20 ± 2.56
3	Rotor	28.84 ± 0.11	9.01 ± 0.46	50.9 ± 10.74	5.42 ± 0.04	415 ± 80.66

**Figure 1.** Surface topography of 100% PET staple (a) ring, (b) airjet, and (c) rotor spun yarns used in the study.

(17.88 turns.inch<sup>-1</sup>). However, due to different yarn formation principles, the true twist in airjet (air-vortex) and rotor yarns cannot be measured.

The physical properties of developed yarns are presented in Table 1 and Figure 1 illustrates the surface topography of the yarns, revealing distinct structural characteristics. Ring yarn exhibits a helical arrangement of fibres in the yarn body. Airjet (air-vortex) yarn displays two fibre arrangements – parallel fibres in the core bound together by wrapper fibres on the yarn surface. Rotor yarn shows bellybands and wild wrapper fibres on its surface. Beyond differences in yarn structure and the various physical properties listed in Table 1, yarn hairiness is an important parameter affecting the textile appearance, durability, handle, and performance during downstream processes and in use. These protruding fibres can be susceptible to damage and fragmentation due to mechanical stresses during manufacturing, use and service of textiles.

The yarn samples for  $\mu$ CT scanning were meticulously prepared by mounting them in the centre of a Kapton® tube (5 mm internal diameter) along its length. An appropriate pretension was applied to ensure the yarns were neither slack nor able to move during scanning. The Zeiss Xradia 620 Versa, located at the National X-Ray Computed Tomography (NXCT) Centre at the University of Manchester, UK, was used to conduct stitched  $\mu$ CT scanning of ring, airjet, and rotor yarns. The X-ray imaging was performed using a Dage sealed transmission source equipped with a tungsten target, which can operate at a tube voltage range of 30–160 kV and a maximum power of 25 W. The system can achieve a minimum spatial resolution of 0.5  $\mu$ m and a minimum voxel size of 0.04  $\mu$ m. The detector system consisted of a charge-coupled device with a 2048 × 2048-pixel array and a physical pixel size of 13.5  $\mu$ m, utilising Cesium Iodate (Thallium) as the detection material. The experimental setup-maintained distances of 9 mm between the detector and sample, and 12 mm between the source and sample. The samples were scanned using a 10× magnification lens at binning one, resulting in 2000 × 2000-pixel projections. This projection diameter of 2000 pixels determined the required number of images per rotation, following the Shannon-Nyquist sampling theorem; therefore, 3201

images were captured per rotation, corresponding to angular steps of 0.112 degrees. Both data acquisition and reconstruction were performed at 16-bit.

The scanning process began by vertically mounting the Kapton® tube on the CT scanning stage with respect to the incident X-ray beam and aligning it along the field of view of the CT scanning system. The stitched scanning technique involved nine consecutive regular scans along the yarn length, with each segment covering more than 1.5 mm and featuring a slight overlap between adjacent segments, as illustrated in Figure 2(c). This stitching approach expanded the field of view during scanning, enabling the acquisition of CT datasets spanning a 12 mm length for each yarn. Figure 2 provides details of the Zeiss Xradia 620 Versa scanning setup, the yarn sample mounted in the Kapton® tube, and the stitched scanning process. The technical specifications for  $\mu$ CT scanning of all three yarn types are presented in Table 2.

An operating voltage of 80 kV was selected to optimise the scanning speed, despite potentially sacrificing some transmission quality. Initial transmission tests of the samples showed values in the high 80% range, notably higher than the optimal transmission range of 20–30% recommended by the system's manufacturer. Subsequent testing at lower voltages (70 kV and 60 kV) revealed only modest decreases in transmission. Given that the sample consisted of two distinct materials – yarn and air – which naturally provided good contrast, the focus was on achieving high-quality images rather than optimising material contrast. While optimising both speed and contrast would have been ideal, the instrument has power limitations at lower voltages which would have necessitated longer exposure times to maintain an acceptable signal-to-noise ratio. Therefore, the decision to

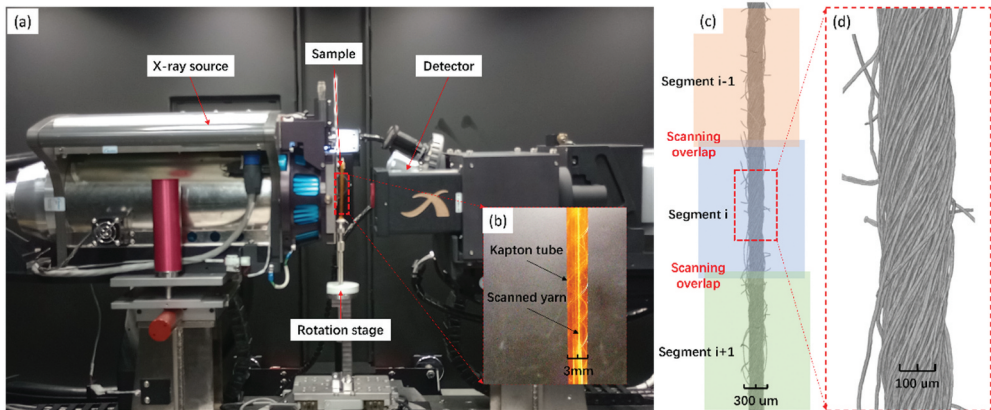


**Figure 2.** (a) Scanning setup of zeiss xradia 620 versa (b) yarn sample prepared in the Kapton tube (c) stitching scans for several segments (d) details of scanned ring-spinning yarn sample.

**Table 2.** Detailed specifications of  $\mu$ CT scanning.

Parameters	Ring yarn	Airjet yarn	Rotor yarn
Resolution/voxel ( $\mu\text{m}$ )	0.790	0.827	0.790
Total CT cross-sectional images along the length	15190	14511	15190
Total scanned length of yarn ( $\mu\text{m}$ )	12000.1	12000.6	12000.1
X-ray energy (KV) * ( $\mu\text{A}$ )	80 * 125	80 * 125	80 * 125
Exposure time (seconds)	3	3	3

operate at 80 kV allowed us to take advantage of higher flux levels from increased wattage, even though this resulted in slightly higher transmission. Even with these optimisations, each frame still required a 3-s exposure time to achieve a satisfactory signal-to-noise ratio.

### 2.1.2. CT dataset stitching

Due to the substantial shifting of the scanning field when transitioning between segments (as illustrated in Figure 3(a)), automatic stitching of CT datasets with nine segments using the Zeiss scanning system software was not feasible. To address this issue, a custom Python algorithm was developed to stitch CT datasets and eliminate overlaps. The initial step in image processing involves noise removal using Median Filter followed by the application of Watershed Separation to generate the binary image for fibre areas, as shown in Figure 3(b,c). The algorithm then analysed the central points of cross-sectional images. For two adjacent segments, a slight overlap of the 10 cross-sectional images (approximately 8 microns in length along the z-axis) was initially introduced. The algorithm further calculated the differences in x-y plane coordinates of the central points

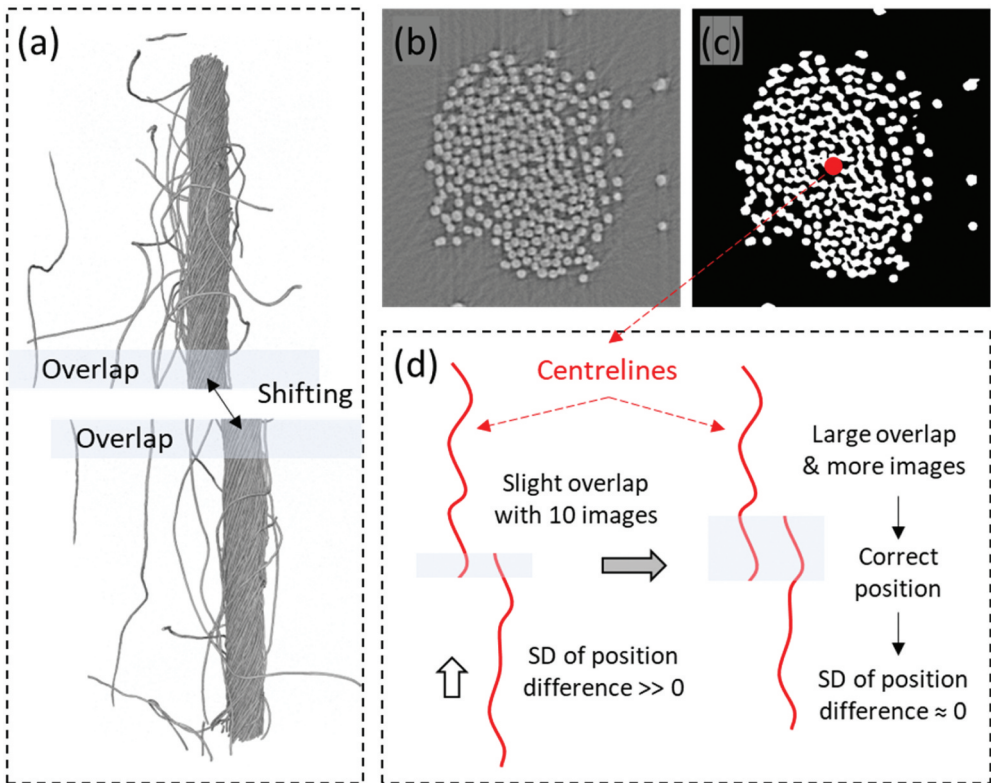


**Figure 3.** Image-processing and micro-ct data integration approach: (a) overlapping regions and positional offsets between consecutive scanned segments, (b) original cross-sectional image, (c) fibre regions after applying threshold and median filter techniques (with central points highlighted in red), (d) identification of the optimal overlap area by minimizing the standard deviation (SD) of positional discrepancies.

between the upper and lower segments within this overlap area (10 differences in the first calculation). The standard deviation of these differences was recorded. The overlap area was then progressively extended with additional cross-sectional images, with each extension yielding a new standard deviation. The correct overlap area was identified when the standard deviation reached a minimum (approaching zero), indicating that the centreline of the upper segment in this overlap area had been translated along the x-y plane to align with the centreline of the lower segment. Since the yarn's centreline is curved at the microscale, a coordinate standard deviation of nearly zero could only be obtained when the overlap area along the z-axis was correctly identified, as shown in Figure 3(d). Using this method, the overlap dataset could be removed, and the coordinates in the x-y plane were adjusted between the two adjacent segments. By applying this technique to stitch two adjacent segments at a time, the CT datasets were merged into a continuous yarn length of 12 mm, facilitating further tracking of individual fibres.

### 2.1.3. Fibre centreline tracking

To track the centreline of each individual fibre, the X-Fibre module of Avizo software was employed, comprising the following four sub-steps:

- (1) Visual Cylinder Template Establishment: A visual cylinder template was created by selecting a fibre segment in a slice and adjusting its length and radius until it fits the cross-section on the slice, as illustrated in Figure 4(a). The 'Cylinder Length'

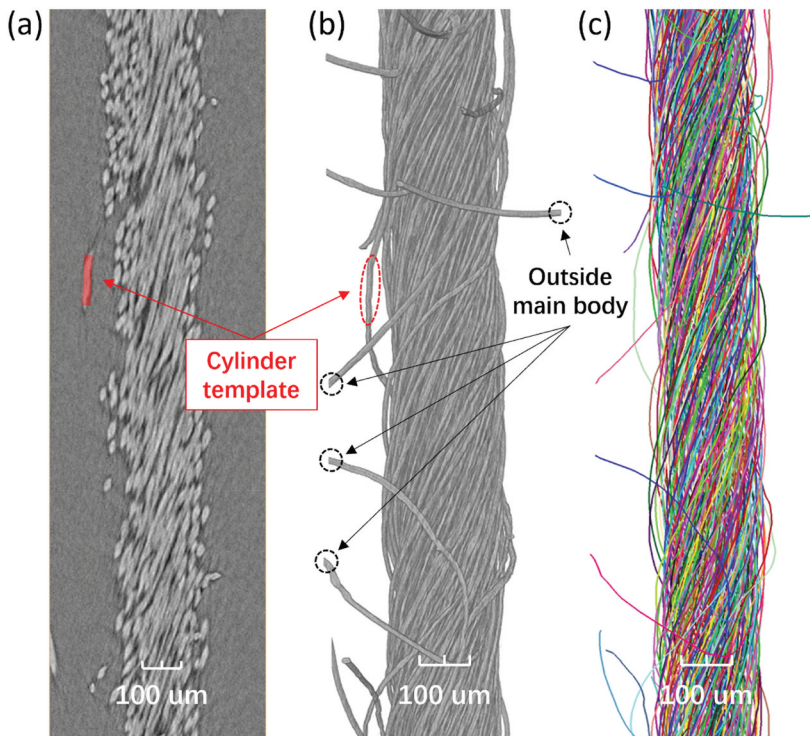


Figure 4. Cylinder template in (a) 2D, (b) 3D view and (c) tracked centrelines for each individual fibre.

**Table 3.** Parameters used in fibre centreline tracking.

Modules in Avizo	Parameters	Value
Cylinder correlation	Cylinder Length ( $\mu\text{m}$ )	20
	Angular Sampling	5
	Mask Cylinder Radius ( $\mu\text{m}$ )	5.5
	Outer Cylinder Radius ( $\mu\text{m}$ )	4
	Inner Cylinder Radius ( $\mu\text{m}$ )	0
Trace Correlation Lines	Minimum Seed Correlation	80
	Minimum Continuation Quality	40
	Direction Coefficient	0.5
	Minimum Distance ( $\mu\text{m}$ )	7
	Minimum Length ( $\mu\text{m}$ )	250
Search Cone	Length ( $\mu\text{m}$ )	30
	Angle (degree)	20
	Minimum Step Size (%)	10

and ‘Angular Sampling’ parameters defined the template’s length and curved angle. Outer and Mask Cylinder Radii set the radius range limits (4 to 6) for cylinder structure detection, with an approximately  $5\ \mu\text{m}$  radius of individual fibre used in this study. The Inner Cylinder Radius was set to 0, as the fibres are solid.

- (2) **Cylinder Correlation:** The Cylinder Correlation module correlated the fibre template with the CT datasets in all orientations, assigning each fibre segment a score (Seed Correlation).
- (3) **Trace Correlation Lines:** This module traced the centrelines of cylinder-like structures. It initiated at a fibre segment with a correlation value exceeding the Minimum Seed Correlation. Two parameters, ‘Minimum Continuation Quality’ and ‘Direction Coefficient’, determined the continuity and directionality when connecting fibre segments into a continuous fibre. To prevent excessive tracking, a minimum distance of  $7\ \mu\text{m}$  was set between two centrelines, and a minimum length of  $250\ \mu\text{m}$  was established to disregard ultra-short centrelines. The Avizo software automatically configured parameters for the Search Cone of centreline connection. All the parameters for these modules are detailed in [Table 3](#).
- (4) **Data Extraction and Compilation:** The Trace Correlation Lines module output Spatial Graph results, as depicted in [Figure 4\(c\)](#). Basic statistics, including chord length, curved length, and coordinates of each point in the centrelines, were extracted from the Spatial Graph and compiled in an MS Excel spreadsheet, associating them with their respective fibre numbers.

## 2.2. Tensile strength of yarns

A universal testing machine (Titan, James Heal) was used to measure the tensile strength of yarns. Twenty specimens from each type of yarn were tested at  $100\ \text{mm}\cdot\text{min}^{-1}$  extension rate and  $250\ \text{mm}$  gauge length using  $5\ \text{kN}$  load cell and results are presented in [Table 5](#).

### 3. Results and discussion

#### 3.1. Analysis of structural arrangement of fibres along the yarn cross section

The cross-sectional analysis provides insights into the structural arrangement of fibres along the yarn cross-section in terms of fibre packing density, radial distribution of fibres (radial packing density), yarn shape factor, and equivalent yarn diameter. As indicated by red arrows in Figure 5(a), hair fibres lie at some distance from the main yarn body and far apart from their neighbouring fibres; these are excluded from the structural analysis.

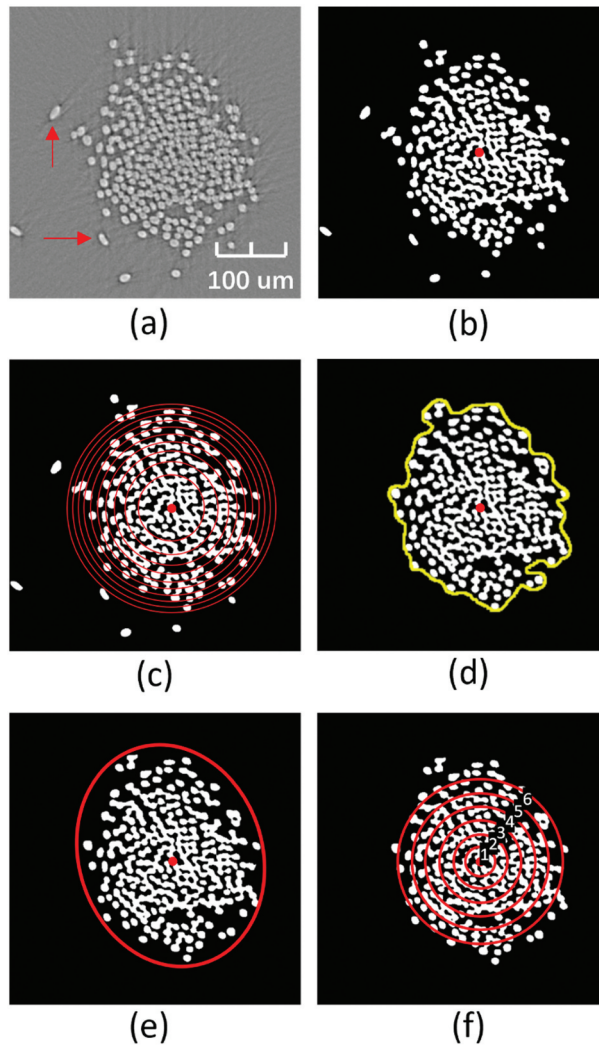


**Figure 5.** The approach of image processing and yarn cross-sectional analysis (using airjet spun yarn as an example): (a) original cross-section with hair fibres (b) fibre areas after threshold and Median Filter (c) division into zones of equal area for hair fibres removal (d) boundary delineation for equivalent yarn diameter (e) ellipse fit for shape factor (f) division into zones of equal radial spacing for radial packing density.

An image processing technique is applied to each cross-sectional image from the CT dataset to first calculate the central point of the yarn and then remove the hair fibres. The initial step involves noise removal using a Median Filter and applying Watershed Separation to obtain a binary image for fibre areas, as shown in [Figure 5\(b\)](#). The central point of the yarn body is calculated using the ‘Measure module’ in Image-J and marked in red. Based on the identified central point, the yarn area is divided into multiple concentric circular regions of equal area, as shown in [Figure 5\(c\)](#), and the packing density of each region is calculated. The initial yarn boundary (after removal of hairs) is defined as the inner radius of the fibres’ region where the packing density of yarn drops below 15%, and individual fibres no longer exist in the form of a fibrous cluster [2]. Fibres located beyond that boundary are treated as hairs and removed from the calculation. The main body of yarn after hair fibre removal is shown in [Figure 5\(d\)](#), with the outer boundary of the main body outlined in yellow.

As the yarn is not perfectly circular, its diameter can be measured from Equation 1 considering equivalent yarn diameter with diameter of an imaginary circle having area exactly equal to the area covered by the yarn body [23].

$$YD_{EQ} = \sqrt{\frac{4 * S_y}{\pi}} \quad (1)$$

Where  $YD_{EQ}$  is the equivalent diameter of yarn and  $S_y$  is the area within the yarn boundary as shown in [Figure 5\(d\)](#).

The fibre packing density can be defined as the ratio of fibres’ area to the total area within the yarn boundary and calculated using Equation 2 [2].

$$DP_f = \frac{S_{tf}}{S_y} \quad (2)$$

Where  $DP_f$  is the fibre packing density and  $S_{tf}$  is the total fibre area (indicated in white in [Figure 5\(d\)](#)).

The yarn shape factor can be calculated from Equation 3 assuming the elliptical shape of yarn from Fit Ellipse Analysis in Image-J (as shown in [Figure 5\(e\)](#)) [23].

$$YS = \frac{L_f}{L_{ma}} \quad (3)$$

Where  $YS$  is the yarn shape factor,  $L_f$  is the distance between the foci of the ellipse and  $L_{ma}$  is the length of the major axis of the ellipse.

Fibre packing density can be represented by the ratio of the area occupied by fibers within the yarn boundary to the total yarn area [30]. This metric helps determine the average packing density of yarn by computing the packing density of fibres in successive cross-sectional zones along the yarn length. Radial packing density represents fibre packing in the yarn as a function of its radius. It provides better insight into how fibres are radially distributed around the yarn centre when the yarn area is divided into circular rings of equal spacing rather than rings of equal area [31]. This approach also aids in investigating the structural arrangement of fibres in a yarn. To calculate the radial packing density, the yarn cross-section is divided into six concentric circular regions of

equal radial spacing. As illustrated in Figure 5(f), six circles are centred with radii of 20, 40, 60, 80, 100, and 120 microns, designated as regions 1 through 6. The radial packing density in each circular/ring region is calculated as the ratio of the fibres' area within it to that region's total area.

The average values of structural parameters (with standard deviation) are presented in Table 4, computed from all CT images (more than 14,500 images for each yarn) along the yarn cross-section. To ensure a fair comparison, the parameters used in image processing are consistent across the three different yarn structures.

The straight and parallel alignment of individual fibres in a yarn allows them to be positioned closer together during yarn formation, resulting in a higher areal packing density within the yarn body. This parameter is found to be higher in ring yarn compared to rotor and air jet yarns. The packing density of ring yarn also appears more uniform along its length, while it is non-uniform in rotor and air jet yarns. This is evident from the standard deviation values presented in Table 4, which indicate greater variation in the cross-sectional measurements of rotor and air jet yarns along their length.

Yarn diameter depends not only on the yarn's linear density and the number of fibres in its cross-section [32] but also on the arrangement and orientation of fibres within the yarn. The calculated equivalent diameter of ring yarn (with the yarn boundary set at 15% packing density threshold) was found to be less than that of rotor and airjet yarns, as shown in Table 4. Since the nominal linear densities of all three yarn types were kept constant in this study, this difference may be attributed to variations in yarn structure, with ring yarn exhibiting better packing and longitudinal orientation of fibres. The lower value of the yarn shape factor indicates a more circular profile in the ring yarn. The shape factor values reveal that none of the yarns have a perfect circular profile. However, the ring yarn has comparatively circular shape, compared to that of rotor and air jet yarns. This is attributed to three different yarn formation principles for the yarns.

The radial distribution of fibres in all three yarn types across different zones along the yarn radius is presented in Table 4 and illustrated in Figure 6. It is evident that the radial packing density (measured as the ratio of fibre area to total area in each circular zone) is

**Table 4.** Results of yarn cross-sectional analysis for three different yarn structures.

Parameters	Ring yarn	Airjet yarn	Rotor yarn
Shape factor	0.42 ± 0.12	0.504 ± 0.127	0.558 ± 0.124
Equivalent yarn diameter (um)	180.31 ± 3.70	207.89 ± 9.72	188.55 ± 14.31
Average fibre packing density (-)	0.57 ± 0.012	0.515 ± 0.02	0.499 ± 0.021
Zone-1 radial packing density (-)	0.6284 ± 0.035	0.598 ± 0.05	0.589 ± 0.05
Zone-2 radial packing density (-)	0.6283 ± 0.023	0.6 ± 0.04	0.589 ± 0.03
Zone-3 radial packing density (-)	0.6254 ± 0.019	0.595 ± 0.03	0.584 ± 0.022
Zone-4 radial packing density (-)	0.5894 ± 0.024	0.534 ± 0.03	0.497 ± 0.03
Zone-5 packing density (-)	0.2634 ± 0.035	0.361 ± 0.07	0.265 ± 0.074
Zone-6 radial packing density (-)	0.0352 ± 0.022	0.128 ± 0.046	0.14 ± 0.059

**Table 5.** Fibre migration parameters and tensile strength of three different yarn structures.

Migration parameters	Ring yarn	Airjet yarn	Rotor yarn
Mean fibre position, $\bar{Y}$ (-)	0.439 ± 0.017	0.40 ± 0.022	0.378 ± 0.027
Mean amplitude of migration (RMS deviation), $\bar{D}$ (-)	0.274 ± 0.008	0.255 ± 0.012	0.251 ± 0.015
Mean migration intensity, $I$ (mm <sup>-1</sup> )	1.91 ± 0.482	4.689 ± 1.363	6.08 ± 2.021
Tensile strength (cN.tex <sup>-1</sup> )	30.51 ± 2.58	25.12 ± 1.66	22.49 ± 1.22

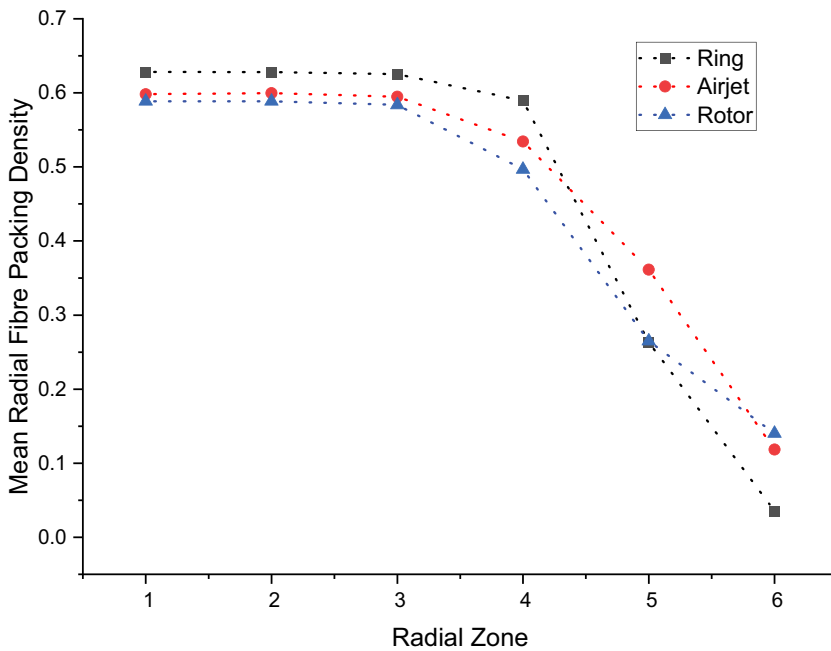


**Figure 6.** Radial packing densities of yarns in different zones along the cross section.

higher around the yarn centre, regardless of yarn type. Each yarn type exhibits a similar radial distribution of fibres up to zone 3, with a slight decrease in zone 4 (which comprises nearly two-thirds of the total yarn cross-sectional area), followed by a sharp decrease in zones 5 and 6. However, the ring yarn demonstrates a higher radial packing density up to zone 4 compared to rotor and airjet yarns, with a sharp decrease in zones 5 and 6. The Tukey's comparison method reveals that the yarn cross-sectional parameters, as presented in Table 4, show statistically significant differences at a 95% confidence level ( $p$ -value = 0.000), except the only insignificant difference of radial packing density at zone-5 ( $p$ -value = 0.110) between ring and rotor yarns.

The outcomes of this analysis may be explained by the differences in yarn formation principles. During ring spinning, the drafted and aligned fibre ribbon at the front drafting roller nip is immediately twisted under variable tension across the fibres, allowing fibres to follow a helical path. Consequently, most fibres are completely embedded in the yarn body with an aligned, helical configuration [33], better fibre extent (the projected fibre length along the yarn axis) [34] and are tightly compressed by helically twisted fibres. This contributes to better packing of fibres near and around the yarn centre, as well as in intermediate zones (zone 3 and 4, Figure 6). This may also result in a smaller diameter and a more regular, round profile of the ring yarn [35]. However, the reduced packing density of fibres in the outer regions of ring-spun yarn (zone 5 and 6, Table 4 and Figure 6) may be attributed to the geometry of spinning triangle at the yarn formation zone. The width of spinning triangle, determined by the drafted strand's width and spinning tension, significantly influences the structural arrangement and distribution of fibres within the yarn. In conventional ring spinning, the larger spinning triangle leads to uneven fibre tension,

causing outer-edge fibres (with higher fibre tension than inner ones) to migrate inward and inner fibres to move outward during yarn formation. This dynamic movement, aimed at balancing fibre tensions, increases the likelihood of edge fibres escaping the full action of twisting and protruding from the yarn body in the form of hairs. Consequently, the radial packing density may decrease sharply towards the outer yarn periphery, while the yarn hairiness increases. The significant reduction of the spinning triangle during compact spinning allows edge fibres to fully integrate into the yarn body, resulting in higher packing density and reduced yarn hairiness [12]. In the case of rotor and air jet yarns, both structures exhibit poorer fibre extent than ring yarn due to technological limitations of their respective spinning systems. For rotor yarn, the lower fibre straightening index of sliver fed to the rotor spinning machine (in contrast to that of roving for ring yarn) and the reassembling of fibres into a free yarn end in the rotor groove leads to fibre buckling and hook formation. This causes an increase in bulkiness and a reduction in fibre packing density [36]. Similarly, the roller drafting of silver mass occurs at a higher speed in the main drafting zone of the air jet spinning machine before yarn formation due to its higher production rate. The fibres are not straightened to the same extent as those in the roving for ring yarn [34]. Additionally, fibres travel a certain distance from the front roller nip to the point of yarn formation (hollow spindle tip) before becoming part of the yarn body, allowing them to relax along their length, leading to decreased fibre packing. Air jet yarn consists of untwisted core fibres encircled by the highest proportion of wrapper fibres and loops of wild fibres, formed by the swirling action of air under minimal tension. These characteristics result in the bulkiest air jet yarn with a greater yarn diameter and higher radial distribution of fibres in the outer zones (zones 5 and 6) compared to ring yarn.

### 3.2. Analysis of structural arrangement of fibres along the yarn length

The fibre migration in the yarns used in this study is analysed by adopting the parameters suggested by Hearle *et al.* [37]. To eliminate hair fibres in 3D space, the distance between each fibre end and the yarn centre is computed. Fibres with one or both ends located beyond the initial yarn radius are designated as hair fibres (adopting the same criteria as in the analysis along the yarn cross-section), as illustrated in Figure 4(b). These hair fibres are excluded from the subsequent fibre migration analyses.

A schematic of fibre segments in yarn is illustrated in Figure 7. All segments of fibre centrelines and the coordinates  $(x_i, y_i, z_i)$  of points on these segments are obtained from the fibre centreline tracking process outlined earlier. The central point  $(x_c, y_c)$  and the yarn radius are derived from the analysis conducted along the yarn cross-section. The description of location variations of fibre segments begins from the fibre position  $Y = (r/R)^2$  along the yarn length, where  $R$  is the yarn radius and  $r = \sqrt{(x_i - x_c)^2 + (y_i - y_c)^2}$  is the distance between the observed fibre segment/point and the centreline of the yarn. The migration parameters, such as mean fibre position ( $\bar{Y}$ ), root mean square (RMS) deviation (mean amplitude of migration,  $\bar{D}$ ), and mean migration intensity ( $I$ ), as proposed by Hearle *et al.* [37] can be expressed as;

Mean fibre position:

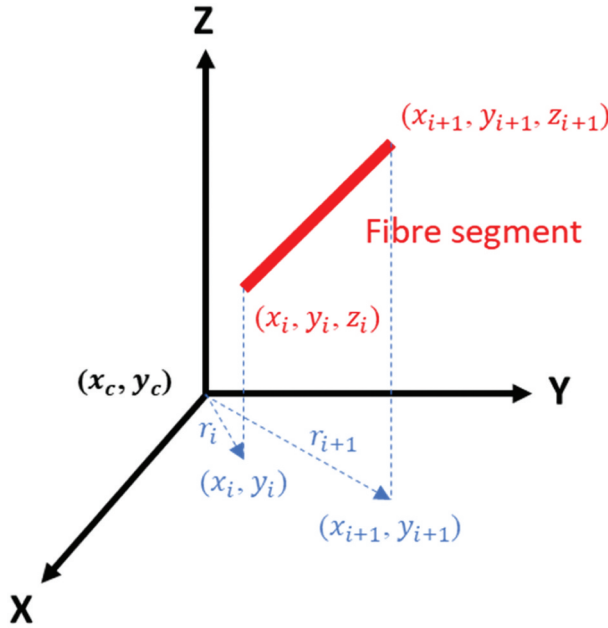


**Figure 7.** A schematic of illustrating the fibre segment in a yarn (adapted from [38]).

$$\bar{Y} = \sum_{i=1}^n \frac{(r/R)^2}{n} \quad (4)$$

Mean Amplitude of Migration (RMS deviation):

$$\bar{D} = \left\{ \sum_{i=1}^{n-1} \frac{(Y_i - \bar{Y})^2}{n} \right\}^{1/2} \quad (5)$$

Mean migration intensity:

$$I = \left[ \sum_{i=1}^{n-1} \left\{ \frac{(Y_{i+1} - Y_i)}{(z_{i+1} - z_i)} \right\}^2 / n \right]^{1/2} \quad (6)$$

where there are  $n$  observations of fibre position  $Y$  along the yarn longitudinal axis  $z_i$ . A MATLAB® program was developed to calculate migration parameters based on the aforementioned equations. The average values of all fibres within the yarn boundary are presented in Table 5. In contrast to the tracer fibre technique, a comprehensive analysis was conducted by calculating all fibre segments within the yarns along their length using tracked centrelines from CT datasets. This approach also ensures a precise and thorough examination of fibre migration and comparative analysis of the three different yarn structures under investigation.

The mean fibre position in a yarn can be represented by averaging the radial positions of continuous fibre segments along its length. This metric indicates the overall tendency of a fibre to be located near the centre or periphery of the yarn. As illustrated in Figure 8 and presented in Table 5, the mean fibre position of ring yarn is higher than both airjet

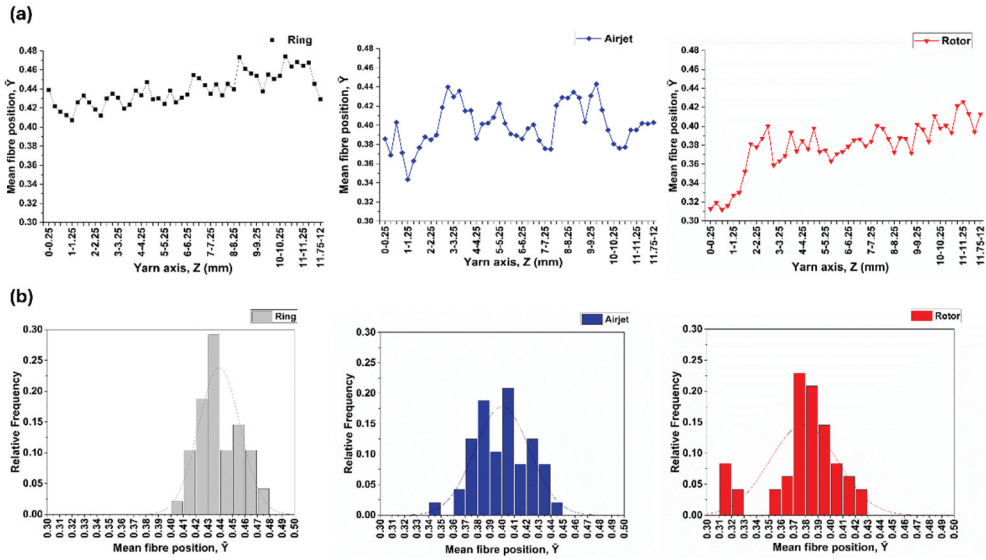


**Figure 8.** Plot of (a) mean fibre position and (b) histograms of mean fibre position.

and rotor yarns, ranging from 0.41 to 0.47. In contrast, this value varies from 0.34 to 0.45 for airjet yarn and 0.31 to 0.43 for rotor yarn, as shown in Figure 8(a). Previous research has reported that a yarn with ideal migration has a mean fibre position value of 0.5 [38]. The histograms in Figure 8(b) and the standard deviation of  $\bar{Y}$  presented in Table 5 indicate a greater dispersion of mean fibre position data for rotor and airjet yarns. These findings suggest an uneven distribution of fibres in rotor and air jet yarns, while ring yarn exhibits a more uniform distribution. A higher value of the mean fibre position also increases the likelihood of fibre ends escaping or appearing near the outer periphery of a yarn, thereby increasing the yarn hairiness [17] which is a distinctive feature of ring-spun yarn.

The amplitude of migration quantifies the extent to which fibres deviate from their mean position within the yarn structure. Research indicates that a yarn exhibiting ideal migration characteristic has a mean amplitude of migration of 0.29 [38]. The Root Mean Square (RMS) deviation, when closer to the ideal value, indicates a greater fluctuation amplitude of fibre segments within yarns. This proximity to the ideal value suggests better self-interlocking of fibres in the yarn structure, and vice versa. Consequently, the amplitude of migration may have a decisive influence on the extent of migration and the tensile properties of yarns.

As shown in Table 5, ring yarn exhibits a mean amplitude of migration closest to the ideal value compared to rotor and air jet yarns. This characteristic favours enhanced self-interlocking of fibres in ring yarn, potentially contributing to higher tensile strength before failure. Conversely, the lower RMS deviation values for rotor and airjet yarns indicate a reduced and more localised extent of migration. This characteristic increases the likelihood of these yarns failing due to fibre slippage during tensile loading, a consequence of poor fibre self-interlocking. This factor, among others, may result in reduced tensile strength.

The mean migration intensity represents the rate of change in the radial positions of fibres. As illustrated in Table 5, rotor and air jet yarns exhibit higher mean migration intensities. This suggests that despite their more localised and lower extent of migration, the fibres in these yarns change their positions more frequently and rapidly compared to those in ring yarn.

The significance values computed using Tukey's comparison method, demonstrate that the differences in mean fibre position, mean amplitude of migration, and mean migration intensity of all three yarn types are statistically significant ( $p$ -values = 0.000) at a 95% confidence level. The only exception is the insignificant difference ( $p$ -value = 0.302) in mean amplitude of migration between rotor and air jet yarns. These results indicate that ring-spun yarn exhibits the highest overall fibre migration, followed by air jet and rotor yarns. Notably, the tensile strength of all three yarns follows the same trend (Table 5): ring > air jet > rotor.

The differences in fibre migration parameters among the three yarn types and their relationship with tensile strength can be attributed to the variations in spinning principles and fibre tensions at yarn formation zones. The higher fibre migration in ring yarn due to higher mean fibre position and amplitude of migration supports better interlocking of the fibres in comparison to airjet and rotor yarns. This contributes to enhanced gripping of fibre bundles offering greater resistance to deformation during tensile loading hence leading to stronger ring yarn. The higher mean fibre position also supports the increase in yarn hairiness [39]. During ring spinning, tension variations on fibres in the drafted ribbon at the twist insertion point force the fibres to migrate within the yarn to balance these tensions. In contrast, fibres are comparatively relaxed with low tension variations at the yarn formation stage in both rotor and air jet yarns, affecting their migration behaviour.

It is interesting to note that the mean fibre position and RMS deviation of air jet yarn are greater than those of rotor yarn, suggesting better fibre migration in air jet yarn compared to rotor yarn. This phenomenon may be explained by the difference in fibre accumulation at the point of yarn formation, despite the lower tension on fibres in both systems. In rotor spinning, the core fibres are twisted in the rotor groove under low tension, resulting in poor fibre extent. The sheath fibres, which enclose the core fibres, are arranged in various helical orientations, forming wild, wrapper, and bellyband fibres. These sheath fibres exhibit almost no migration due to their distinct positioning and the spinning process characteristics [17,33]. In air jet spinning, the yarn structure consists of core fibres predominantly encased by wrapper fibres. As these wrapper fibres swirl around the hollow spindle tip, their leading ends are likely to integrate into the core, while their trailing ends continue to whirl around the core, maintaining their wrapper fibre status. This dynamic process potentially allows wrapper fibres a greater opportunity to migrate from the core to the yarn surface. Consequently, airjet yarns exhibit improved mean fibre position and RMS deviation compared to rotor yarns, indicating enhanced fibre migration.

### 3.3. Contextual review of fibre migration parameters

Table 6 summarises and compares the fibre migration parameters and packing density of ring, rotor, and airjet yarns with those reported in the literature. A significant variation in

**Table 6.** Summary of published literature on structural analysis of spun yarns and comparison with the current study.

Reference	Method used	Yarn type	Yarn count (tex)	Twist level (tpm)	Staple fibres used	Mean fibre position ( $\bar{Y}$ )	RMS deviation ( $\bar{D}$ )	Mean migration intensity, $\text{mm}^{-1}$ ( $I$ )	Migration factor ( $K = \bar{D} * I$ ) [38]	Mean Fibre Packing density (-)
[17]	Tracer fibre	Ring spun	57.9 (10.2's Ne)	503.02	Cotton	0.49	0.27	3.82	1.03	-
[40]	Tracer fibre	Ring spun	29.53 (20's Ne)	581	Lyocell	0.58	0.20	1.31	0.262	-
[12]	Tracer fibre	Ring spun	21.09 (28's Ne)	833.30	Cotton	0.32	0.16	2.57	0.4112	-
[38]	Tracer fibre	Ring spun	19.7 (30's Ne)	862.55	Cotton	0.42	0.24	2.41	0.58	-
[17]	Tracer fibre	Rotor spun	60.3 (9.8's Ne)	-	Cotton	0.40	0.23	3.05	0.70	-
[20]	Tracer fibre	Airjet spun	21.09 (28's Ne)	-	Cotton	0.30	0.20	2.80	0.56	-
[23]	$\mu$ CT	Ring spun	12 (49.22's Ne)	1108	Cotton	0.31	0.43	1.61	0.69	0.499
[21]	Cross-section microtomy	Ring spun	19.7 (30's Ne)	797.86	Lyocell	-	-	-	-	0.38
[41]	Cross-section microtomy	Ring spun	19.8 (29.83's Ne)	730	Lyocell	-	-	-	-	0.531
[42]	Cross-section microtomy	Ring spun	23.62 (25's Ne)	689	Lyocell	-	-	-	-	0.603
[21]	Cross-section microtomy	Airjet spun	19.7 (30's Ne)	-	Lyocell	-	-	-	-	0.24
[41]	Cross-section microtomy	Rotor spun	21.5 (27.47's Ne)	747	Lyocell	-	-	-	-	0.413
This study	$\mu$ CT	Ring spun	29.53 (20's Ne)	703.93	Polyester (PET)	0.439	0.274	1.91	0.523	0.57
This study	$\mu$ CT	Rotor spun	29.53 (20's Ne)	-	Polyester (PET)	0.378	0.251	6.08	1.526	0.499
This study	$\mu$ CT	Airjet spun	29.53 (20's Ne)	-	Polyester (PET)	0.40	0.255	4.69	1.196	0.515

structural parameters is observed even among yarns produced using the same spinning principle. This variability may be attributed to factors beyond the yarn formation system, such as fibre properties (cross-sectional shape, fineness, flexibility, length, etc.) and process parameters (twist, draft, type of fed material, etc.). Furthermore, the limitations inherent in tracer fibre technique and cross-sectional microtomy is likely to influence the results.

An important parameter to consider is the ‘migration factor’, introduced in a study [38], which is calculated by multiplying the RMS deviation and mean migration intensity to represent the total migration in a yarn. Interestingly, when calculating the migration factor for yarns in the current study, the total migration is highest in rotor yarn, followed by airjet and ring yarns. A product of higher RMS deviation value with lower migration intensity may result in less total migration, while a product of low RMS deviation with higher migration intensity may lead to greater total migration. A yarn with higher values of both RMS deviation and mean migration intensity might exhibit better total migration. It can be argued that a yarn with higher RMS deviation may have a more significant impact on the extent of migration and self-interlocking of fibres compared to yarn with greater mean migration intensity. While the introduced ‘migration factor’ parameter [38] may be useful in determining total migration when comparing yarns spun with the same type of spinning principle, it might be misleading when comparing yarns produced by different spinning technologies due to fundamental differences in their spinning principles.

### **3.4. Relationship of structural parameters with released FFs mass**

The results of FFs mass released and collected from bespoke textiles (produced using the same yarns under study, as published in [8]) after successive laundry cycles in the laboratory are presented in Figure 9. As discussed in detail in previous study [8], ring-spun fabrics release higher mass of FFs compared to airjet and rotor fabrics. The cumulative mass of FFs collected from all washing cycles reveals that airjet and rotor samples release 28% (avg. FFs mass: 0.67 mg/g textile) and 33% (avg. FFs mass: 0.63 mg/g textile) less mass, respectively, compared to ring-spun samples (avg. FFs mass: 0.94 mg/g textile). Since yarn and fabric production parameters were kept consistent, except for differences in yarn production methods, these outcomes may be attributed to variations in ring, airjet, and rotor yarn structures, as examined in detail in the current study using  $\mu$ CT.

The higher release of FFs from ring-spun fabrics may be linked to yarn hairiness, as indicated by higher Zweigle hairiness S3 and Uster hairiness index values (Table 1). Despite higher fibre migration and mean fibre packing density in ring yarns, the sharp decrease in radial fibre packing density in zones 5 and 6 (the peripheral yarn layers) compared to airjet and rotor yarns (Figure 6 and Table 4) provides a secondary explanation. Yarn hairiness and radial distribution of fibres (radial packing density) in these peripheral regions may be closely related to FFs mass release. Specifically, higher yarn hairiness and lower radial fibre packing density in the outer regions contribute to increased FFs mass release and vice versa. This may be attributed to the increased susceptibility of fabrics, with hairy ring yarns and loosely packed fibres in the peripheral zones, to easy fibre damage from external forces during manufacture and use, leading to

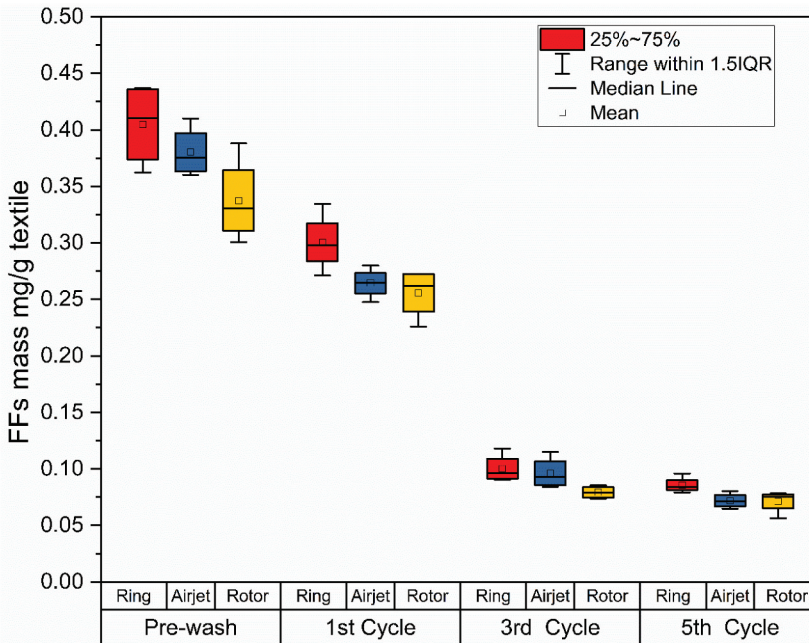


**Figure 9.** Fragmented fibres (FFs) mass collected from wash effluent after pre-wash, 1st, 3rd and 5th laundry cycles. The plot of data is based on quadruplicate experiments [8].

enhanced generation and release of FFs. Furthermore, the freedom of movement and escape of already existing FFs from the textile structure may not be restricted due to the aforementioned reasons. These outcomes highlight that the structural features of yarns, especially the hairiness and radial packing density of fibres in the peripheral regions, are critical to the generation and release of FFs from textiles. Therefore, it can be reasoned that the loosely packed and hairy fibres at the yarn surface contribute to higher FFs mass release and vice versa [43]. For the first time,  $\mu$ CT has been employed to characterise the microstructure of three commercially and industrially relevant yarn structures, and the relevance of yarn microstructural parameters to the release of fragmented fibres.

#### 4. Conclusion

For the first time, micro-computed tomography was employed to scan and investigate the structure of 100% polyester ring, rotor, and airjet staple spun yarns (commercially and industrially most common yarns) along their length and cross-section simultaneously in a non-invasive manner and link the yarn structural parameters with FFs mass release from corresponding textiles. The  $\mu$ CT approach overcame the limitations associated with traditional methods such as tracer fibre technique and cross-sectional microtomy. Cross-sectional analysis revealed that the ring yarn exhibited a rounder profile with a smaller diameter and higher fibre packing density compared to airjet and rotor yarns. Additionally, ring yarn demonstrated higher mean fibre position and migration amplitude, followed by airjet and rotor yarns, indicating a greater extent of fibre migration. However, the mean

migration intensity of the ring yarn was lower than both airjet and rotor yarns. Despite higher fibre migration and mean fibre packing density, the higher release of FFs from ring-spun textiles was attributed to greater yarn hairiness and lower radial fibre packing density in the peripheral regions of yarn, compared to airjet and rotor-spun yarns. Statistical analysis confirmed significant differences in structural parameters among the three types of yarns. A direct relationship was observed between fibre migration parameters (mean fibre position and migration amplitude), mean fibre packing density, and tensile strength of yarns. This relationship followed the order of ring > airjet > rotor, with the stronger ring spun yarn exhibiting higher values of mean fibre position, migration amplitude, and mean fibre packing density, followed by airjet and rotor yarns.

### Disclosure statement

No potential conflict of interest was reported by the author(s).

### Funding

The Engineering and Physical Sciences Research Council (EPSRC) of UK under the grant reference number [EP/T024542/1 and EP/T02464X/1] financially supported this work.

### References

- [1] Engelhardt AW. Global development of spun and filament yarns. 2019 2019 Dec 4.
- [2] Zheng S, Zou Z, Shen W, et al. A study of the fiber distribution in yarn cross section for vortex-spun yarn. *Text Res J.* 2012;82(15):1579–1586. doi: [10.1177/0040517511431315](https://doi.org/10.1177/0040517511431315)
- [3] Tyagi G. Yarn structure and properties from different spinning techniques. *Advances in yarn spinning technology*. Cambridge: Woodhead Publishing; 2010. p. 119–154.
- [4] Basal G. The structure and properties of vortex and compact spun yarns. Raleigh: North Carolina State University; 2003.
- [5] Lawrence CA. *Fundamentals of spun yarn technology*. 1st ed. Boca Raton (FL): CRC Press; 2003.
- [6] Herbert S. *The rieter manual of spinning-volume 6: alternative spinning systems*. Winterthur: Schwabe AG; 2018.
- [7] Jabbar A, Palacios-Marín AV, Ghanbarzadeh A, et al. Impact of conventional and modified ring-spun yarn structures on the generation and release of fragmented fibers (microfibers) during abrasive wear and laundering. *Text Res J.* 2022;93(5–6):1099–1112. doi: [10.1177/00405175221127709](https://doi.org/10.1177/00405175221127709)
- [8] Jabbar A, Tausif M. Investigation of ring, airjet and rotor spun yarn structures on the fragmented fibers (microplastics) released from polyester textiles during laundering. *Text Res J.* 2023;93(21–22):5017–5028. doi: [10.1177/00405175231191785](https://doi.org/10.1177/00405175231191785)
- [9] Peirce F. Geometrical principles applicable to the design of functional fabrics. *Text Res J.* 1947;17(3):123–147. doi: [10.1177/004051754701700301](https://doi.org/10.1177/004051754701700301)
- [10] Morton W, Yen K. 37—Fibre arrangement in cotton slivers and laps. *J Text Inst Trans.* 1952;43(9):T463–T72. doi: [10.1080/19447025208659689](https://doi.org/10.1080/19447025208659689)
- [11] Neckář B, Ishtiaque S, Švehlová L. Rotor yarn structure by cross-sectional microtomy. *Text Res J.* 1988;58(11):625–632. doi: [10.1177/004051758805801102](https://doi.org/10.1177/004051758805801102)
- [12] Basal G, Oxenham W. Comparison of properties and structures of compact and conventional spun yarns. *Text Res J.* 2006;76(7):567–575. doi: [10.1177/0040517506065591](https://doi.org/10.1177/0040517506065591)

- [13] Guo Y, Tao X, Xu B, et al. Structural characteristics of low torque and ring spun yarns. *Text Res J.* 2011;81(8):778–790. doi: [10.1177/0040517510387213](https://doi.org/10.1177/0040517510387213)
- [14] Yilmaz D, Göktepe F, Göktepe Ö, et al. Packing density of compact yarns. *Text Res J.* 2007;77(9):661–667. doi: [10.1177/0040517507078796](https://doi.org/10.1177/0040517507078796)
- [15] Sinha SK, Kumar P, Ghosh S. Study on the packing density of structurally modified ring spun yarn. *Fib Polym.* 2016;17(11):1898–1907. doi: [10.1007/s12221-016-5940-y](https://doi.org/10.1007/s12221-016-5940-y)
- [16] Soltani P, Johari M. A study on siro-, solo-, compact-, and conventional ring-spun yarns. Part I: structural and migratory properties of the yarns. *J Text Inst.* 2012;103(6):622–628. doi: [10.1080/00405000.2011.595567](https://doi.org/10.1080/00405000.2011.595567)
- [17] Huh Y, Kim YR, Oxenham W. Analyzing structural and physical properties of ring, rotor, and friction spun yarns. *Text Res J.* 2002;72(2):156–163. doi: [10.1177/004051750207200212](https://doi.org/10.1177/004051750207200212)
- [18] Ganesan S, Ramakrishnan G. Fibre migration in compact-spun yarns: part I—pneumatic compact yarn. *Ind J Fib Text Res.* 2006;31(03):381–386. <http://nopr.niscpr.res.in/handle/123456789/24532>
- [19] Hearle J, Lord P, Senturk N. 43—fibre migration in open-end-spun yarns. *J Text Inst.* 1972;63(11):605–617. doi: [10.1080/00405007208630383](https://doi.org/10.1080/00405007208630383)
- [20] Basal G, Oxenham W. Effects of some process parameters on the structure and properties of vortex spun yarn. *Text Res J.* 2006;76(6):492–499. doi: [10.1177/0040517506064253](https://doi.org/10.1177/0040517506064253)
- [21] Kilic M, Buyukbayraktar RB, Kilic GB, et al. Comparing the packing densities of yarns spun by ring, compact and vortex spinning systems using image analysis method. *Ind J Fib Text Res.* 2014;39(04):351–357. <http://nopr.niscpr.res.in/handle/123456789/30097>
- [22] Jiang X, Hu J, Cheng K, et al. Determining the cross-sectional packing density of rotor spun yarns. *Text Res J.* 2005;75(3):233–239. doi: [10.1177/004051750507500308](https://doi.org/10.1177/004051750507500308)
- [23] Haleem N, Liu X, Hurren C, et al. Investigating the cotton ring spun yarn structure using micro computerized tomography and digital image processing techniques. *Text Res J.* 2019;89(15):3007–3023. doi: [10.1177/0040517518805387](https://doi.org/10.1177/0040517518805387)
- [24] Toda M, Grabowska K, Ciesielska-Wróbel I. Application of micro-computed tomography (micro-ct) to study unevenness of the structure of yarns. *Text Res J.* 2017;87(3):351–368. doi: [10.1177/0040517516629149](https://doi.org/10.1177/0040517516629149)
- [25] Toda M, Grabowska KE. Computed microtomography in the analysis of fiber migration in yarn. *Aut Res J.* 2013;13(1):28–32. doi: [10.2478/v10304-012-0020-x](https://doi.org/10.2478/v10304-012-0020-x)
- [26] Pandita SD, Verpoest I. Prediction of the tensile stiffness of weft knitted fabric composites based on X-ray tomography images. *Comp Sci Technol.* 2003;63(2):311–325.
- [27] Shinohara T, Takayama J-Y, Ohyama S, et al. Extraction of yarn positional information from a three-dimensional CT image of textile fabric using yarn tracing with a filament model for structure analysis. *Text Res J.* 2010;80(7):623–630. doi: [10.1177/0040517509342320](https://doi.org/10.1177/0040517509342320)
- [28] Vicente MA, Mínguez J, González DC. The use of computed tomography to explore the microstructure of materials in civil engineering: from rocks to concrete. In: Ahmet MH, editor. *Computed Tomogr-Adv Appl.* 2017. p. 207–230. doi:[10.5772/intechopen.69245](https://doi.org/10.5772/intechopen.69245).
- [29] Podgorsak AR. Use of electron-multiplying charge-coupled device based micro-ct system for pre-clinical medical imaging applications. State University of New York at Buffalo; 2017.
- [30] Eldessouki M, Ibrahim S. Chan-veze segmentation model for faster and accurate evaluation of yarn packing density. *Text Res J.* 2016;86(2):167–177. doi: [10.1177/0040517514557314](https://doi.org/10.1177/0040517514557314)
- [31] Hearle JW, Grosberg P, Backer S. *Structural mechanics of fibers, yarns, and fabrics*: Wiley-interscience. New York: Wiley-Interscience; 1969.
- [32] Slater K. Yarn evenness. *Text Prog.* 1986;14(3–4):1–90.
- [33] Soe AK, Takahashi M, Nakajima M, et al. Structure and properties of MVS yarns in comparison with ring yarns and open-end rotor spun yarns. *Text Res J.* 2004;74(9):819–826. doi: [10.1177/004051750407400911](https://doi.org/10.1177/004051750407400911)
- [34] Ishtiaque S, Salhotra K, Kumar A. Analysis of spinning process using the Taguchi method. Part II: effect of spinning process variables on fibre extent and fibre overlap in ring, rotor and air-jet yarns. *J Text Inst.* 2006;97(4):285–294.

- [35] Kilic GB, Okur A. A comparison for the physical properties of cotton, modal and acrylic yarns spun in ring and OE-rotor spinning systems/comparatie între proprietatile fizice ale firelor de bumbac, modale si acrilice filate în sistemele cu inele si cu capat liber OE. *Indus Text.* 2016;67(2):81.
- [36] Mohamed M, Lord P, Saleh H. A comparison of the hairiness and diameter of ring and open-end yarns. *Text Res J.* 1975;45(5):389–395. doi: [10.1177/004051757504500505](https://doi.org/10.1177/004051757504500505)
- [37] Hearle J, Gupta B, Merchant V. Migration of fibers in yarns: part I: characterization and idealization of migration behavior. *Text Res J.* 1965;35(4):329–334. doi: [10.1177/004051756503500407](https://doi.org/10.1177/004051756503500407)
- [38] Huh Y, Kim YR, Ryu WY. Three-dimensional analysis of migration and staple yarn structure. *Text Res J.* 2001;71(1):81–89. doi: [10.1177/004051750107100113](https://doi.org/10.1177/004051750107100113)
- [39] Singh C, Gordon S, Zhang S, et al. A new insight into the dynamics of fibre migration in ring spinning. *J Text Inst.* 2019;110(4):552–561. doi: [10.1080/00405000.2018.1496587](https://doi.org/10.1080/00405000.2018.1496587)
- [40] Li SY, Fu H. Image analysis and evaluation for internal structural properties of cellulosic yarn. *Cellulose.* 2021;28(10):6739–6756. doi: [10.1007/s10570-021-03900-z](https://doi.org/10.1007/s10570-021-03900-z)
- [41] Ishtiaque S. Radial packing density of rotor-and ring-spun yarns. *Ind J FibText Res.* 1986;11(04):208–214. <http://nopr.niscpr.res.in/handle/123456789/32912>
- [42] Salehi M, Johari MS. Study of fiber packing density of lyocell ring-spun yarns. *J Text Inst.* 2011;102(5):389–394. doi: [10.1080/00405000.2010.482341](https://doi.org/10.1080/00405000.2010.482341)
- [43] Jabbar A, Palacios-Marín AV, Ghanbarzadeh A, et al. Impact of conventional and modified ring-spun yarn structures on the generation and release of fragmented fibers (microfibers) during abrasive wear and laundering. *Text Res J.* 2023;93(5–6):1099–1112. doi: [10.1177/00405175221127709](https://doi.org/10.1177/00405175221127709)